Draft version November 14, 2022
Typeset using LaTeX twocolumn style in AASTeX62

The Density Profiles of Collapsed Rotating Massive Stars Favor Long Gamma-Ray Bursts

Goni Halevi,[1,2] Belinda Wu,[1] Philipp Mösta,[3] Alexander Tchekhovskoy,[4] Ore Gottlieb,[4] and David R. Aguilera-Dena[5]

[1] *Department of Astrophysical Sciences, Princeton University, 4 Ivy Lane, Princeton, NJ 08544, USA*
[2] *Institute For Advanced Study, 1 Einstein Drive, Princeton, NJ 08540, USA*
[3] *GRAPPA, Anton Pannekoek Institute for Astronomy and Institute of High-Energy Physics, University of Amsterdam, Science Park 904, 1098 XH Amsterdam, The Netherlands*
[4] *Center for Interdisciplinary Exploration & Research in Astrophysics (CIERA), Physics & Astronomy, Northwestern University, Evanston, IL 60201, USA*
[5] *Institute of Astrophysics, FORTH, Dept. of Physics, University of Crete, Voutes, University Campus, GR-71003 Heraklion, Greece*

(Received XX; Revised XX; Accepted XX)

Submitted to ApJL

ABSTRACT

Long-duration gamma-ray bursts (lGRBs) originate in relativistic collimated outflows – jets – that drill their way out of collapsing massive stars. Accurately modeling this process requires realistic stellar profiles for the jets to propagate through and break out of. Most previous studies have used simple power laws or pre-collapse models for massive stars. However, the relevant stellar profile for lGRB models is in fact that of a star after its core has collapsed to form a compact object. To develop such stellar profile, we use the one-dimensional open-source code GR1D to simulate the core-collapse process for a suite of low-metallicity, rotating, massive stellar progenitors that have undergone chemically homogeneous evolution. The models we evolve span a range of zero-age main sequence (ZAMS) masses: $M_{\rm ZAMS}$ = 13, 18, 21, 25, 35, 40, and 45 $M_\odot$. We follow four out of our seven models until they collapse to form black holes (BHs), while the other three form proto-neutron stars (PNSs). We robustly find, across all models, that the final density profile outside of the newly formed BH or PNS is well-represented by a power law with an index of $\alpha \approx 1.2 - 1.5$. Density profiles with these indices are conducive to successful formation, propagation, and breakout of BH-powered jets and, in fact, required to reproduce observable properties of lGRBs. Future models of lGRBs should be initialized according to shallower *post-collapse* stellar profiles like those presented here instead of the much steeper pre-collapse profiles that are typically used.

Keywords: magnetohydrodynamics — stellar mass black holes — gamma-ray bursts — core-collapse supernovae

1. INTRODUCTION

Evolved, massive stars that undergo core-collapse are commonly accepted as the progenitors of luminous, energetic transient sources including long-duration gamma-ray bursts (lGRBs) and core-collapse supernova (CCSN) explosions. The environments of lGRBs – star-forming, preferentially low-metallicity galaxies – suggest a link to the core-collapse process (e.g. Bloom et al. 2002). Individual lGRBs detected to be coincident with Type Ic-bl SNe (e.g. Modjaz et al. 2006; Galama et al. 1998), hydrogen- and helium-deficient explosions feature broad spectral features, bolster the 'SN-GRB' connection between the central engines driving these events (Modjaz et al. 2016). The favored model for this engine is the collapsar scenario (MacFadyen & Woosley 1999). Under this framework, the iron core of a massive star collapses to a Kerr black hole (BH) without driving a successful SN explosion. Afterwards, the high angular momentum of the stellar envelope leads to disk formation and the BH accretes matter, enabling energy to be extracted as

Corresponding author: Goni Halevi
ghalevi@princeton.edu

Poynting flux (Blandford & Znajek 1977). This process leads to the launching of a relativistic, collimated outflow – a jet – that clears its path out of the star and breaks out of the envelope to eventually be observed as a burst of beamed, energetic gamma rays.

Evolved, massive Wolf-Rayet (WR) stars are theoretically the most likely evolutionary channel to lead to collapsars as their significant wind-driven mass loss results in depleted stellar envelopes for jets to break out of (Woosley 1993). WR stars are also associated with highly stripped (Type Ic) SNe (e.g. Gal-Yam et al. 2014; Dessart et al. 2017), like those that are observationally linked to lGRBs. Similar stars that fail to form BHs may also successfully power lGRBs and SNe Ic-BLs through the proto-magnetar model (Metzger et al. 2011; Shankar et al. 2021). Relativistic hydrodynamical simulations combined with radiation transport calculations have demonstrated that the central engine of a lGRB can trigger a SN Ic-BL in a WR star, jointly producing both observed phenomena from the same massive stellar progenitor (Barnes et al. 2018).

A subset of SNe Ic known as Type I superluminous supernovae (SLSNe) have also been proposed to have similar origins to lGRBs (e.g. Lunnan et al. 2014; Angus et al. 2016; Aguilera-Dena et al. 2018; Margalit et al. 2018) based on both theoretical and observational evidence. SLSNe exhibit intrinsic luminosities one to two orders of magnitude greater than those of "normal" SNe (see Gal-Yam 2012; Moriya et al. 2018, for reviews). Their spectral signatures point to progenitors that have undergone severe mass loss and/or mixing phases (Mazzali et al. 2016; Gal-Yam 2019), while their extreme luminosities suggest a source of power in addition to the radioactive decay of ^{56}Ni that powers other SNe. WR stars that fail to form BHs but instead leave behind millisecond magnetars are proposed to power these SLSNe (SLSNe; Kasen & Bildsten 2010; Woosley 2010; Metzger et al. 2015; Nicholl et al. 2017) by continuously depositing energy into the ejecta during spin-down.

Numerical studies of lGRBs (see Lazzati et al. 2015, for a review) often manually ignite a jet in the center of a stellar profile and then follow its evolution to calculate observables like light curves and spectral signatures. In many of these simulations (e.g Morsony et al. 2007; Lazzati et al. 2012; López-Cámara et al. 2013, 2016; Barnes et al. 2018; Xie & MacFadyen 2019), the stellar profiles are pre-collapse WR stars that represent lGRB progenitors, primarily the commonly-used 16TI model of Woosley & Heger (2006a). The choice of these stellar models assumes that the process that leads to BH or protomagnetar formation leaves the rest of the star unaffected.

Recent three-dimensional (3D) general-relativistic magnetohydrodynamical (GRMHD) simulations (Gottlieb et al. 2022a,b) are the first to self-consistently launch a jet through accretion onto a Kerr BH and follow its journey through the stellar envelope, spanning the large spatial and temporal range necessary to study the observable jet properties. By exploring a range of stellar density profiles represented by analytic power-laws rather than simply assuming a fit to 16TI, these simulations showed that the steepness of the density profile constrains the jet's physical properties (Gottlieb et al. 2022a). In particular, Gottlieb et al. (2022a) find that only profiles that are significantly shallower than 16TI and other similar pre-collapse WR stars are compatible with observations of lGRBs.

In this Letter, we investigate the core-collapse process in massive stars motivated as lGRB progenitors and their post-collapse properties. In §2, we describe the properties of the models we evolve and our numerical setup for doing so. We report the results from our core-collapse simulations, including the remnants and density profiles in §3. We end by discussing the consequences of these results in the context of lGRBs and encouraging future models to use physically-motivated stellar profiles in §4.

2. METHODS

In this work, we present results from simulations of the core-collapse of massive stars and investigate their evolution and final, post-collapse states.

2.1. *Pre-collapse stellar models*

The initial conditions for our core-collapse simulations are drawn from the stellar evolution models described in Aguilera-Dena et al. (2020) (hereafter AD20). We now summarize the basic physics of the AD20 suite of models.

AD20 presents the evolution, until the onset of core-collapse, of stellar progenitors across the initial mass range for massive, low-metallicity stars, spanning zero-age main sequence (ZAMS) masses of $M_{\rm ZAMS} = 4 - 45 M_\odot$. The models are computed using the open-source one-dimensional (1D) stellar evolution Modules for Experiments in Stellar Astrophysics in version 10398 (MESA; Paxton et al. 2011, 2013, 2015, 2018). Each star is initialized with (1) a rapid equatorial rotational velocity of 600 km s^{-1} and (2) a low metallicity of $(1/50)Z_\odot$, where $Z_\odot$ represents solar metallicity and abundances are scaled from Grevesse et al. (1996). The fast initial rotation guarantees effective mixing leading to quasi-chemically homogenous evolution. These models, which result in fast-rotating pre-collapse cores with hydrogenand helium-depleted envelopes, are motivated as potential progenitors of lGRBs, and SLSNe (Aguilera-Dena et al. 2018, AD20) or SNe Ic-BL.

We evolve seven different models from the set of 42 included in AD20, spanning a range of initial masses and expected explosion properties. We choose the $M_{\rm ZAMS} = 18 M_\odot$ model as our fiducial model because it is most similar, at the onset of core-collapse, to the well-studied lGRB progenitor model 16Ti of Woosley & Heger (2006b). It has a similar mass of $14.15 M_\odot$ (compared to $13.95 M_\odot$ for 16Ti) at the onset of core collapse due to mass loss dominated by rotation, which is enhanced by neutrino-driven contraction. The $M_{\rm ZAMS} = 18 M_\odot$ stellar model is classified by AD20 as a likely failed supernova and potential lGRB progenitor based on various explosion criteria. The simplest of these is the core-compactness parameter, ξ_M, which is motivated by hydrodynamic simulations of neutrino-driven SNe and defined as

$$\xi_M = \frac{M/M_\odot}{R(M) = M)/1000\ \rm km}, \quad (1)$$

where $R(M)$ is the radius of the enclosed baryonic mass M (O'Connor & Ott 2011). This single-parameter estimate is commonly used as an indicator of 'explodability'– whether or not a non-rotating stellar core will lead to a successful neutrino-driven explosion. It is often measured at a mass coordinate of $2.5\ M_\odot$, which corresponds to a typical infall velocity of $1000\ \rm km\ s^{-1}$. Non-rotating cores with $\xi_{2.5} \gtrsim 0.45$ are predicted to be difficult to successfully explode, as calibrated by core-collapse simulations (Sukhbold & Woosley 2014). Our fiducial model has $\xi_{2.5} = 0.62$. All of the models we present here, except for the lowest mass ($M_{\rm ZAMS} = 13 M_\odot$) one, have compactness parameters above 0.45 and are therefore expected by this simple explodability predictor to fail to explode and to instead collapse to form BHs.

Figure 1 shows radial profiles of density, temperature, radial velocity, and angular velocity at this time for the fiducial $M_{\rm ZAMS} = 18 M_\odot$ model along with the other six models. We include the initial parameters for each of these models, as taken from AD20, in the first few columns of Table 1. In particular, we list the stellar mass at the onset of core-collapse (defined as the time when the core infall velocities first exceed $1000\ \rm km\ s^{-1}$) $M_{\rm pre-cc}$ and the compactness parameter $\xi_{2.5}$. We note that while there are many similarities between the different models, there are also non-linear differences between them, for example in the rotational velocities of their core regions (see Figure 1d). This is also reflected in the non-monotonic (as a function of stellar mass) behavior of $\xi_{2.5}$.

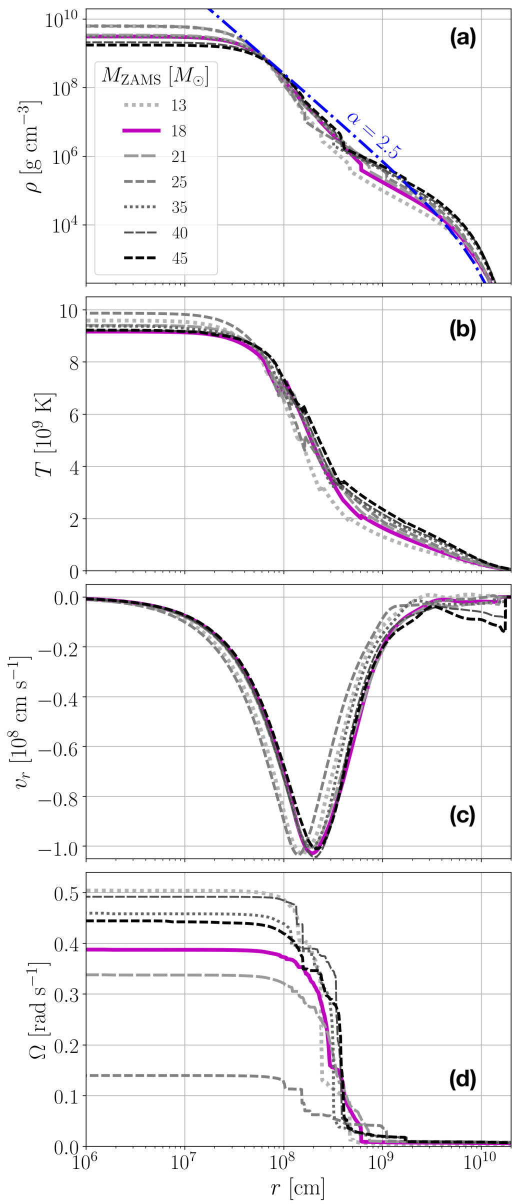

Figure 1. Stellar properties as a function of radius for the 1D MESA models of Aguilera-Dena et al. (2020). In the four panels, we show (a) mass density, (b) temperature, (c) radial velocity, and (d) angular velocity. The different mass models are represented by different color and style lines as labeled, with the fiducial $M_{\rm ZAMS} = 18 M_\odot$ model in solid magneta. We also include, in blue, a fit to Equation 2 with $\alpha = 2.5$. All models share similar density, temperature, and radial velocity profiles. Their core rotational velocities differ by factors of a few and vary non-monotonically with ZAMS mass.

Besides the $13 M_\odot$ one, all of the models we adopt fail to meet the explosion criterion of Müller et al. (2016), which predicts properties of neutrino-driven explosions based on a semi-analytic model for stellar structure. Both the least ($13 M_\odot$) and most massive ($45 M_\odot$) mod-

$M_{\rm ZAMS}$ ($M_\odot$)	$M_{\rm pre-cc}$ ($M_\odot$)	$\xi_{2.5}$	$t_{\rm bounce}$ (ms)	t_f (ms)	$M_{\rm core}$ ($M_\odot$)	α
13	10.37	0.21	152	835	2.03	1.42
18	14.15	0.62	234	741	2.45	1.45
21	16.39	0.66	216	719	2.44	1.40
25	19.33	0.47	152	767	2.08	1.28
35	26.53	0.57	247	825	2.40	1.24
40	30.08	0.78	258	735	2.68	1.41
45	33.59	0.85	285	614	2.63	1.50

Table 1. Parameters of the stellar models. We take the following pre-collapse quantities directly from AD20: ZAMS mass $M_{\rm ZAMS}$, mass at the time of re-mapping to GR1D $M_{\rm pre-cc}$, and compactness parameter at this time $\xi_{2.5}$ as defined in Equation 1. We add to these the time of core-bounce in our GR1D simulations $t_{\rm bounce}$ and final quantities at the end of the simulation, which occurs at t_f: the mass of the inner core $M_{\rm core}$ and best-fit power-law index for the density profile α.

els are predicted to explode based on the Ertl et al. (2016) test, which employs a two-parameter representation of stellar structure, while the rest fail to meet this criterion as well. These predictions are also not monotonic with initial or pre-collapse mass due to the complexities of stellar evolution. We include the $M_{\rm ZAMS} = 13M_\odot$ model as a comparison point to the failed supernovae, but from the perspective of likely lGRB progenitors, we focus on the more massive models.

2.2. *Core-collapse simulations*

We map each of the pre-collapse models onto GR1D (GR1D; O'Connor & Ott 2010), another spherically-symmetric code, in order to evolve through the final stage of stellar evolution. GR1D is an open-source tool[1] for simulating core-collapse and BH formation. It uses a finite-volume scheme with piecewise-parabolic reconstruction and a Riemann solver to solve the discretized equations of general-relativistic hydrodynamics (GRHD). It couples with microphysical, tabulated equations of state and includes an approximate treatment of rotation that makes it effectively 1.5D. It too is a modular code and, crucially, implements neutrino transport in the M1 formulation (O'Connor 2015) with tabulated multi-group neutrino opacities. Spherically symmetric models can never fully capture the inherently multi-dimensional properties of stars (e.g. critically-rotating stars are expected to be significantly oblate) and their collapse process (e.g. Müller 2016; O'Connor & Couch 2018). However, for the purpose of approximating a collapsing star's remnant mass, and averaged radial thermodynamic profiles rather, GR1D is a useful and sufficient tool (e.g. O'Connor & Ott 2010, 2011; O'Connor et al. 2018). GR1D allows us to simulate the entire star rather than collapsing only the inner-region, which is critical for understanding the environment that a collimated outflow from the accreting newborn compact object must propagate through and break out of in order to power a lGRB.

The initial conditions for our GR1D simulations are the pre-collapse models of AD20. Each model is remapped from MESA once it has reached a maximum core infall velocity of $v_r > 1000$ km s^{-1}, representing the onset of core-collapse. The masses of the stars at this time, $M_{\rm pre-cc}$ are included in the third column of Table 1. In particular, we map the following parameters (as a function of radial coordinate) onto a new grid: enclosed mass, temperature, density, radial velocity, electron fraction, and angular velocity. We choose a grid in GR1D that is uniform ($\Delta r = 100$ m) in the inner region (up to 2 km) and logarithmically spaced outside of it, with a total of 1200 radial zones (in addition to ghost zones). The grid extends out to where the density has dropped below $\rho_{\rm min} = 2000$ g cm^{-3}, corresponding to a typical radius of $r(\rho = \rho_{\rm min}) \approx (0.8-1)\times 10^{10}$ cm. This minimum density does not effect the evolution of the star during collapse; the grid we use captures the overwhelming majority ($> 80\%$ by mass) of each star, and the parts of the envelope at $r \gtrsim 10^9$ cm ($\rho \lesssim 10^5$ g cm^{-3}) are unchanged during core-collapse (see Fig. 2).

We choose a commonly-used tabulated equation of state (EOS) appropriate for hot nuclear matter from Lattimer & Swesty (1991) with an incompressibility of $K_{\rm sat} = 220$ MeV (known as LS220). We include 3 species of neutrinos and evolve them out to 600 km. Their opacities are tabulated and include 18 energy groups and a large parameter space of thermodynamic quantities.

3. RESULTS

3.1. *Core-collapse evolution*

The fiducial $M_{\rm ZAMS} = 18M_\odot$ model along with the $M_{\rm ZAMS} = 21$, 40, and 45 $M_\odot$ ones all collapse to form BHs. Every model in this set follows similar evolution. On the other hand, the $M_{\rm ZAMS} = 13$, 25, and 35 $M_\odot$ models all fail to form BHs and may be representative of successful neutrino-driven supernova explosions. To represent these two different outcomes, we show the density and radial velocity profiles for the $M_{\rm ZAMS} = 18$ and 13 $M_\odot$ models at multiple stages of their evolution in Figure 2.

[1] https://github.com/evanoconnor/GR1D

During collapse, the outer envelope of the star ($r \gtrsim 4\times 10^{10}$ cm) is largely unaffected due to causality, while the inner region falls inward, making the core increasingly compact. Nuclear and strong forces in the dense core lead to the production of a proto-neutron star (PNS) and drive a shock outward at at time $t_{\rm bounce}$ (known as core-bounce). We include snapshots from just before and just after this time in Figure 2.

At $t < t_{\rm bounce}$, infalling material steepens into a shock and there is a sharp drop in density outside the core and a correspondingly sharp negative velocity at the same radius ($r \approx 10$ km). At $t > t_{\rm bounce}$, the shock moves outward as neutrinos are released in the core and heat the region behind it. This is reflected in the positive velocities at the boundary of the newly formed PNS and then outward movement of the shock.

Eventually, however, the shock stalls and falls back, leading to the infall of the shock as seen in Figure 2 for the $M_{\rm ZAMS} = 18$ and 13 $M_\odot$ models. For the former, our fiducial model, core-bounce occurs at $t_{\rm bounce} = 234$ ms. Approximately half a second later, the PNS itself begins to collapse to form a BH, marking the end of the simulation. This is reflected in a rapid increase of the density in the inner regions and negative radial velocities appearing within the PNS boundary. We end our simulations at this time because GR1D can no longer evolve the metric once the central density exceeds a certain level (dependent on the choice of metric). We list the times of core bounce $t_{\rm bounce}$ and the final simulation time t_f for all models in Table 1.

3.2. *Remnants*

The central density as a function of time after core-bounce is shown for each simulation in the top panel of Figure 3. For all models, the core density grows steadily after bounce as the core continues to accrete mass. The maximum PNS mass is a function of both the EOS and the angular momentum of the core. The cores of the $M_{\rm ZAMS} = 18M_\odot$, $21M_\odot$, $40M_\odot$, and $45M_\odot$ models all accrete enough matter to experience runaway gravitational collapse of the PNS. At this point, the central density rises exponentially and surpasses physical values as the core mass exceeds the maximum allowed NS mass, indicating the onset of BH formation. At this stage, the GR1D simulation ends as it cannot continue to evolve the metric to a true singularity.

In each of our seven models, a shock wave is driven outward from the core at the time of core-bounce. However, it stalls and turns back within 100 ms for all models as fallback accretion occurs. The $M_{\rm ZAMS} = 13$ and 25 $M_\odot$ models both experience a brief shock revival from neutrino heating but still eventually undergo a reversal and fallback accretion, as seen in the inset in the middle panel of Figure 3. These two models also have the smallest enclosed mass within the shock radius and the lowest pre-collapse compactness parameters (see Table 1).

The inner core mass $M_{\rm core}$ is defined as the mass within the radius at which the radial velocity first exceeds the sound speed, $r_{\rm shock}$. While $M_{\rm core}$ increases throughout the duration of our simulations, the rate at which it does so decreases for all models as accretion slows and $r_{\rm shock}$ asymptotes. Each model forms a core of mass $2M_\odot < M_{\rm core} < 2.7M_\odot$ by the end of the simulation, as shown in both Table 1 and the bottom panel of Figure 3. In all cases, $M_{\rm core}$ represents the minimum mass for the final remnants, as the cores are expected to continue accreting matter after the end of our simulations.

The $M_{\rm ZAMS} = 35M_\odot$ model also fails to collapse to a BH by the end of our simulations. These outcomes suggest a critical core-compactness parameter of $\xi_2.5 \approx 0.6$, with models that are more compact than this value collapsing to BHs in our GR1D simulations. However, it is possible that in longer or multi-dimensional simulations, some of the models that we do not see collapse in GR1D would do so. This is especially likely for the $M_{\rm ZAMS} = 35M_\odot$ model, which has the most massive core (as seen in Table 1 as well as the bottom panel of Figure 3) and the greatest pre-collapse compactness parameter (0.57) of the non-BH-forming models.

3.3. *Density profiles*

For each of the seven simulations, we find that the density profile after core-collapse is well-fit by a distribution of the form:

$$\rho(r) = \rho_0 \left(\frac{r}{r_g}\right)^{-\alpha} \left(1 - \frac{r}{R_\star}\right)^3 \qquad (2)$$

where ρ_0 is the normalization factor satisfying $M_\star = \int_0^{R_\star} \rho(r) dV$, r_g is the gravitational radius of the remnant, and $R_\star$ is the stellar radius.

The initial density profiles are similar across stellar masses with best-fit power-law indices of $\alpha \approx 2.5$. In all cases, the density profile becomes shallower during core-collapse, and especially in the time after the shock stalls and turns around. The final density and pressure profiles are very smooth in the region 20 km $\lesssim r \lesssim$ 2000 km. For our fiducial collapsed stellar model at the end of the GR1D simulation, we find a best-fit value of $\alpha = 1.45$ for the density outside of the BH event horizon. We include the best-fit value of α for all models in the final column of Table 1. They vary non-monotonically with mass, though clearly trend steeper for higher values of core-compactness $\xi_{2.5}$, and range from 1.24 for the

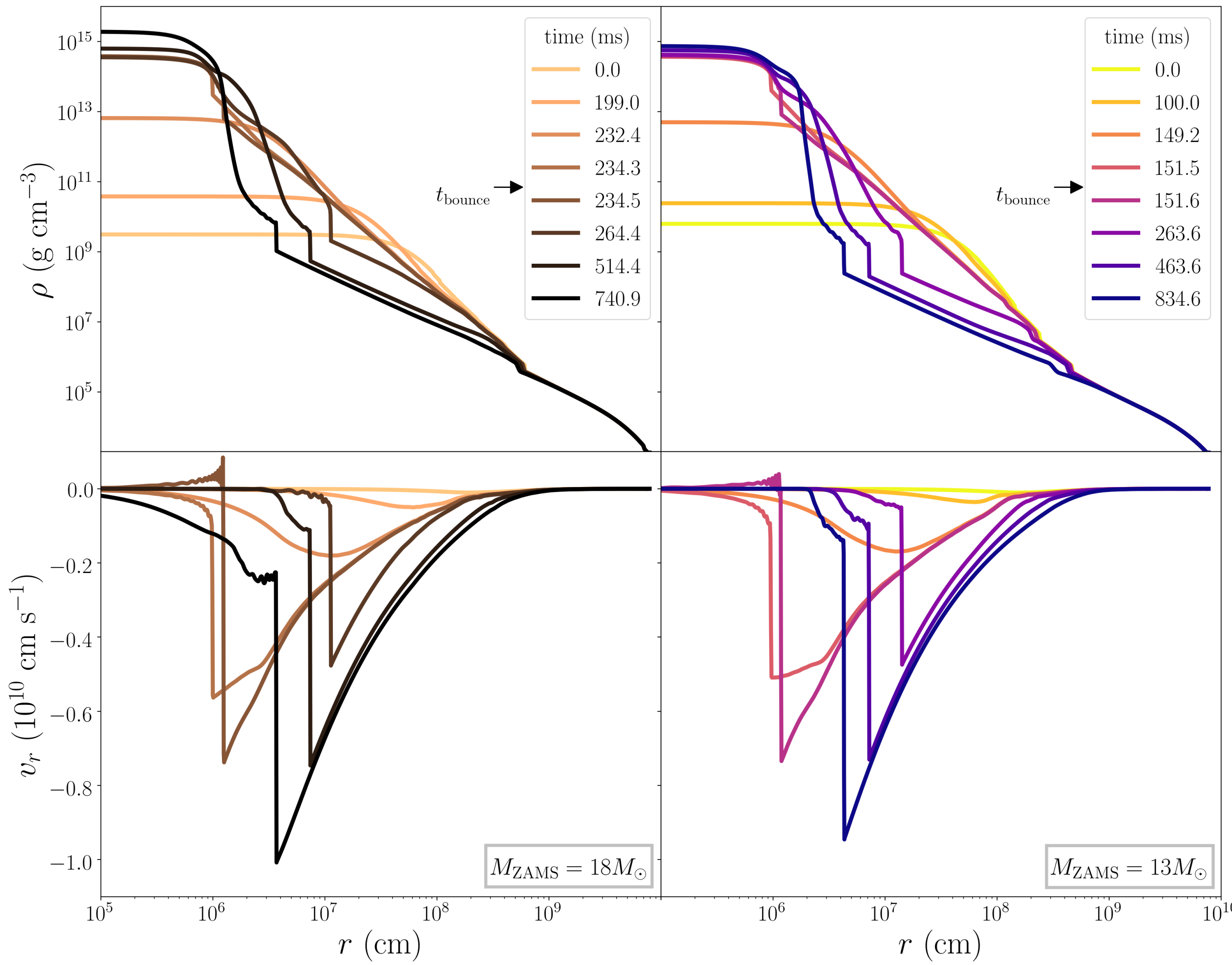

Figure 2. Evolution of the density and velocity profiles (in top and bottom panels, respectively) of the $M_{\rm ZAMS} = 18M_\odot$ and $13M_\odot$ models (left and right, respectively) during GR1D evolution through core collapse. In the bottom left panel, there is infall within the core (at $r < 10^6$ cm) in the final snapshot for the $18M_\odot$ model, but no such infall in the final state of the $13M_\odot$ model. This is evidence that the core of the $18M_\odot$ model collapses to a BH at the end of its evolution, whereas the core of the $13M_\odot$ model remains a PNS.

$M_{\rm ZAMS} = 35M_\odot$ model to 1.50 for the $M_{\rm ZAMS} = 45M_\odot$ model. We compare the density profiles for all seven models at the beginning and end of their GR1D simulations in Figure 4.

4. DISCUSSION AND CONCLUSION

Power-law density profiles with indices of $\alpha \approx 1.5$ are consistent with the simple case of free-fall acceleration outside the core. The pressure distributions after core-collapse are well-fit with slightly steeper power-laws ($p_{post-cc} \propto r^{-1.8}$) across all models, reflecting the steeper initial distributions in pressure ($p_{pre-cc} \propto r^{-4}$). These post-collapse distributions are also consistent with free-fall. This makes it all the more meaningful that the GR1D simulations we perform yield this robust result for the final state of all models. The initial models have non-linear differences in their stellar structure, so there are complicated variations in the inputs to GR1D. These differences are mainly related to whether core carbon burning proceeds radiatively or convectively.

Meanwhile, the physics that enters these 1D simulations is complex in that we simulate collapse in full general-relativity, with multi-group neutrino transport and realistic tabulated equations of state suitable for dense matter. Simulations that do not include neutrino transport produce dramatically different results, with post-collapse density profiles that are significantly steeper, reflecting the pre-collapse state. This suggests that neutrinos radiated from the core play an important role in shaping the thermodynamic evolution of the stel-

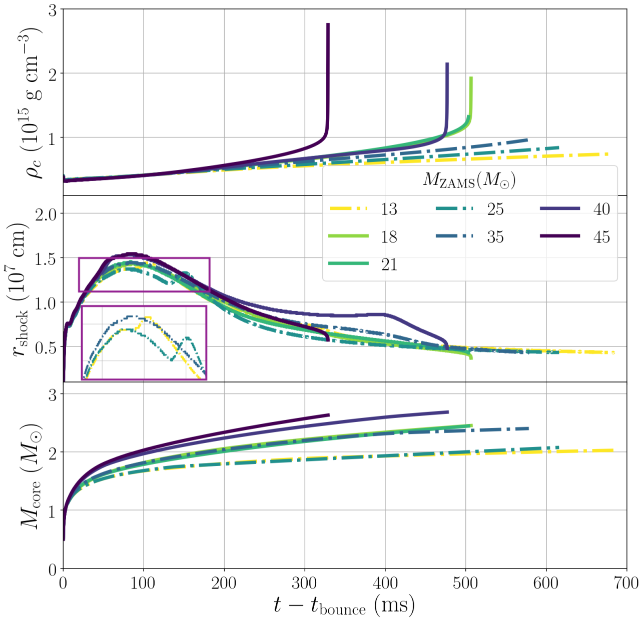

Figure 3. Evolution of several key quantities (from top to bottom: central density, shock radius, and mass of the inner core) with time after core bounce for all seven models. The shock radius $r_{\rm shock}$ is defined as the place where the radial velocity exceeds the sound speed and the inner core is the region within this radius, so $M_{\rm core} \equiv M(r < r_{\rm shock})$. Models that form BHs in our simulations are represented by solid lines while models that do not are shown as dash-dotted lines. The inset in the middle panel zooms in on the shock radius evolution for the three models that do not form BHs, two of which experience a brief shock revival stage.

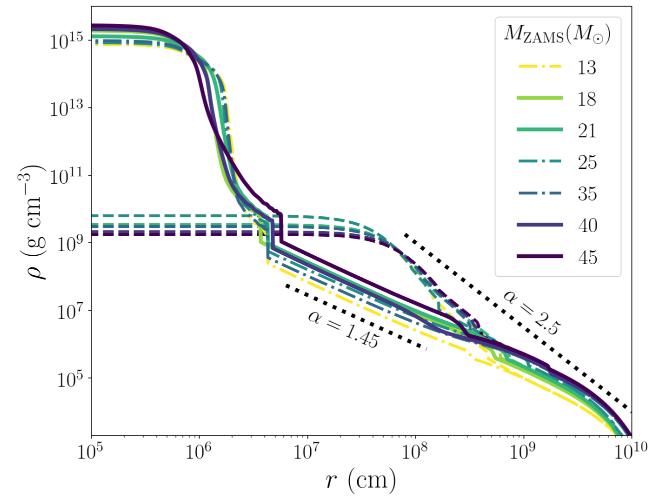

Figure 4. Initial (pre-core-collapse) and final density profiles for all seven stellar models. Initial profiles are shown as dashed lines. For the final profiles, we use solid lines for models that collapse to form BHs in our simulations and dash-dotted lines for those that do not. Representative power-law scalings with indices of 2.5 and 1.45 are shown in dotted black lines for comparison to initial and final profiles, respectively.

lar envelope. The superficially simple outcome we find – post-collapse stellar profiles outside the PNS or BH closely approximate those predicted by free-fall acceleration – is thus all the more surprising.

We note that for the set of models we evolve, there is a positive correlation between core-compactness $\xi_{2.5}$ and the steepness of the final density profile. It remains to be seen whether this holds for a broader range of stellar evolution models rather than only those with low metallicities and rapid rotation that experience wind-driven mass loss and significant mixing, as is typical of lGRB progenitors.

4.1. *Applications for lGRBs*

The consequences of the precise density profiles we find in our 1D core-collapse simulations of real stellar progenitor models are favorable for producing long GRBs. 3D GRMHD simulations of collapsars have followed the formation and break-out of jets (Gottlieb et al. 2022a,b). These simulations begin with idealized initial conditions of a central BH surrounded by an effectively zero-temperature star represented by an analytic power-law density profile as in Equation 2. Dipolar magnetic fields and fast rotational velocities are then added to the idealized stellar profile, leading to accretion, a build-up of magnetic flux at the horizon, and the launching of a jet that propagates through the stellar envelope. Gottlieb et al. (2022a) varied the initial power-law index α and compared the physical quantities inferred from the resulting jets to observational constraints. They conclude that inner stellar density profiles with indices of $0.5 \lesssim \alpha \lesssim 1.5$ may be responsible for producing the full range of long GRB observables. In particular, such profiles are found to be necessary to produce jets with the proper luminosities, and (flat) evolution in jet power with time. On the other hand, density profiles like those of pre-collapse models 16Ti (Woosley & Heger 2006b) or the pre-collapse models of AD20 have steeper profiles of $\alpha \approx 2.5$. Such profiles require too luminous of jets to overcome accretion and break out – $L \gtrsim 10^{52}$ erg s^{-1}. They also produce time-evolving accretion rates, which in turn translate to evolving jet luminosities (Gottlieb et al. 2022a). These properties are in tensions with observations of lGRBs.

Here we have shown that commonly-used pre-collapse lGRB progenitor models (e.g. 16TI of Woosley & Heger 2006a) with density profiles that have power-law indices of $\alpha \approx -2.5$ naturally lead to post-collapse profiles with $\alpha \lesssim 1.5$. We will present results from 3D GRMHD simulations of jet launching, propagation, and breakout through post-collapse stellar profiles with realistic thermodynamic properties in future work (Halevi et al. ????, in prep.). We emphasize that for consistency and physical accuracy, future numerical studies and theoretical models of lGRBs should consider post-collapse stellar models as the material through which lGRB jets evolve.

We thank Evan O'Connor for helpful discussions and advice about using GR1D. We also thank Jim Stone, Eliot Quataert, and Elias Most for helpful discussions. G.H. is supported in part by a National Science Foundation Graduate Research Fellowship.

Software: GR1D (O'Connor & Ott 2010; O'Connor 2015), Matplotlib (Hunter 2007).

REFERENCES

Aguilera-Dena, D. R., Langer, N., Antoniadis, J., & Müller, B. 2020, ApJ, 901, 114
Aguilera-Dena, D. R., Langer, N., Moriya, T. J., & Schootemeijer, A. 2018, ApJ, 858, 115
Angus, C. R., Levan, A. J., Perley, D. A., et al. 2016, MNRAS, 458, 84
Barnes, J., Duffell, P. C., Liu, Y., et al. 2018, ApJ, 860, 38
Blandford, R. D., & Znajek, R. L. 1977, MNRAS, 179, 433
Bloom, J. S., Kulkarni, S. R., & Djorgovski, S. G. 2002, AJ, 123, 1111
Dessart, L., Hillier, D. J., Yoon, S.-C., Waldman, R., & Livne, E. 2017, A&A, 603, A51
Ertl, T., Janka, H. T., Woosley, S. E., Sukhbold, T., & Ugliano, M. 2016, ApJ, 818, 124
Gal-Yam, A. 2012, Science, 337, 927
—. 2019, ApJ, 882, 102
Gal-Yam, A., Arcavi, I., Ofek, E. O., et al. 2014, Nature, 509, 471
Galama, T. J., Vreeswijk, P. M., van Paradijs, J., et al. 1998, Nature, 395, 670
Gottlieb, O., Lalakos, A., Bromberg, O., Liska, M., & Tchekhovskoy, A. 2022a, MNRAS, 510, 4962
Gottlieb, O., Liska, M., Tchekhovskoy, A., et al. 2022b, ApJL, 933, L9
Grevesse, N., Noels, A., & Sauval, A. J. 1996, in Astronomical Society of the Pacific Conference Series, Vol. 99, Cosmic Abundances, ed. S. S. Holt & G. Sonneborn, 117
Halevi, G., Gottlieb, O., Mösta, P., et al. ????
Hunter, J. D. 2007, Computing in Science and Engineering, 9, 90
Kasen, D., & Bildsten, L. 2010, ApJ, 717, 245
Lattimer, J. M., & Swesty, D. F. 1991, NuPhA, 535, 331
Lazzati, D., Morsony, B. J., Blackwell, C. H., & Begelman, M. C. 2012, ApJ, 750, 68
Lazzati, D., Morsony, B. J., & López-Cámara, D. 2015, Journal of High Energy Astrophysics, 7, 17
López-Cámara, D., Lazzati, D., & Morsony, B. J. 2016, ApJ, 826, 180
López-Cámara, D., Morsony, B. J., Begelman, M. C., & Lazzati, D. 2013, ApJ, 767, 19
Lunnan, R., Chornock, R., Berger, E., et al. 2014, ApJ, 787, 138
MacFadyen, A. I., & Woosley, S. E. 1999, ApJ, 524, 262
Margalit, B., Metzger, B. D., Thompson, T. A., Nicholl, M., & Sukhbold, T. 2018, MNRAS, 475, 2659
Mazzali, P. A., Sullivan, M., Pian, E., Greiner, J., & Kann, D. A. 2016, MNRAS, 458, 3455
Metzger, B. D., Giannios, D., Thompson, T. A., Bucciantini, N., & Quataert, E. 2011, MNRAS, 413, 2031
Metzger, B. D., Margalit, B., Kasen, D., & Quataert, E. 2015, MNRAS, 454, 3311
Modjaz, M., Liu, Y. Q., Bianco, F. B., & Graur, O. 2016, ApJ, 832, 108
Modjaz, M., Stanek, K. Z., Garnavich, P. M., et al. 2006, ApJL, 645, L21
Moriya, T. J., Sorokina, E. I., & Chevalier, R. A. 2018, SSRv, 214, 59
Morsony, B. J., Lazzati, D., & Begelman, M. C. 2007, ApJ, 665, 569
Müller, B. 2016, PASA, 33, e048
Müller, B., Heger, A., Liptai, D., & Cameron, J. B. 2016, MNRAS, 460, 742
Nicholl, M., Guillochon, J., & Berger, E. 2017, ApJ, 850, 55
O'Connor, E. 2015, ApJS, 219, 24
O'Connor, E., & Ott, C. D. 2010, Classical and Quantum Gravity, 27, 114103
—. 2011, ApJ, 730, 70
O'Connor, E., Bollig, R., Burrows, A., et al. 2018, Journal of Physics G Nuclear Physics, 45, 104001
O'Connor, E. P., & Couch, S. M. 2018, ApJ, 865, 81
Paxton, B., Bildsten, L., Dotter, A., et al. 2011, ApJS, 192, 3
Paxton, B., Cantiello, M., Arras, P., et al. 2013, ApJS, 208, 4
Paxton, B., Marchant, P., Schwab, J., et al. 2015, ApJS, 220, 15
Paxton, B., Schwab, J., Bauer, E. B., et al. 2018, ApJS, 234, 34

Shankar, S., Mösta, P., Barnes, J., Duffell, P. C., & Kasen, D. 2021, MNRAS, 508, 5390
Sukhbold, T., & Woosley, S. E. 2014, ApJ, 783, 10
Woosley, S. E. 1993, ApJ, 405, 273
—. 2010, ApJL, 719, L204
Woosley, S. E., & Heger, A. 2006a, ApJ, 637, 914
—. 2006b, ApJ, 637, 914
Xie, X., & MacFadyen, A. 2019, ApJ, 880, 135